Chalcogenide Distribution in Microporous Layered Tin(IV) Thioselenide, TMA$_2$Sn$_3$S$_x$Se$_{7-x}$, Materials

Homayoun Ahari, Ömer Dag, Srebri Petrov, and Geoffrey A. Ozin*

Materials Chemistry Research Group, Lash Miller Chemistry Department, 80 St. George Street, University of Toronto, Toronto, Ontario M5S 3H6, Canada

Robert L. Bedard

UOP, 25 Algonquin Road, Des Plaines, Illinois

Received: November 21, 1997; In Final Form: January 20, 1998

The synthesis and characterization of 15 ternary microporous layered tin(IV) thioselenide, TMA$_2$Sn$_3$S$_x$Se$_{7-x}$, materials (where $0 \leq x \leq 7$), enabled the chalcogenide distribution in the framework to be defined. The structure of the materials is based upon the apex and edge connection of three trigonal bipramidal SnS$_y$Se$_{5-y}$ building blocks (where $0 \leq y \leq 5$) into a broken-cube cluster. Six of these clusters are linked together into a planar honeycomb layer arrangement of hexagonally shaped 24-atom rings that are stacked together in a parallel manner to form the microporous layered lattice. An understanding of the chalcogenide distribution necessitated a combination of powder X-ray diffraction (PXRD), and UV−vis diffuse-reflectance, FT-Raman, and ^{1}H/^{119}Sn CP/MAS NMR spectroscopies. PXRD established the arrangement of chalcogenides in the porous layers, UV−vis diffuse-reflectance spectroscopy determined the organization at the level of the clusters, while FT-Raman and NMR spectroscopies elucidated the local distribution around the trigonal bipyramids. By investigation of the TMA$_2$Sn$_3$S$_x$Se$_{7-x}$ structure at these different length scales, it was found that the chalcogenide distribution is statistical at the global level of the unit cell but displays site selectivity at the local level of the trigonal bipyramids.

Introduction

Trigonal bypyramidal (TB) SnX$_5$ is the primary building unit of a class of microporous layered tin(IV) chalcogenides, formulated as R$_2$Sn$_3$X$_7$, and denoted as SnX-1, where X = S or Se and R is a space-filling organic cation.[1] These materials are unique among all known open-frameworks in that their structure is based solely on distorted TBs, comprised of two long axial and three short equatorial tin−chalcogenide bonds each having a slightly different length (Figure 1a). One way to describe the overall structure of R$_2$Sn$_3$X$_7$ begins with the connection of three TBs through a common axial apex and three apex−equatorial edges to create a broken-cube cluster, referred to as the secondary building unit (Figure 1b). Six of these clusters are further linked together through two TB axial and equatorial dangling bonds that are located at the three symmetry-equivalent cube apexes to form an anionic planar honeycomb layer arrangement of hexagonally shaped 24-atom rings, called the tertiary building unit (Figure 1c). The layer topology can be described as a 2,2,3-connected 2-D net of TB SnX$_5$ building units, which in TB notation can be written as [Sn(X$_{ax}$)$_{1/3}$(X$_{ax}$)$_{1/2}$(3X$_{eq}$)$_{1/2}$]. Parallel packing of the anionic [Sn$_3$X$_7$]$^{2-}$ layers produces the quaternary structure of the microporous layered tin(IV) chalcogenides (Figure 1d). Charge-balancing organic cations reside within intralayer pores and interlayer spaces. A range of organic molecules are able to template R$_2$Sn$_3$X$_7$; however, each structure is found to be geometrically unique because cooperative interactions between the layers and organic molecules cause particular intralayer angular distortions, bond-length alterations, different layer-stacking arrangements, and distinct interlayer spacings.[1] This

is the origin of the elasticity of the structure and the polymorphism observed for R$_2$Sn$_3$X$_7$. The flexibility allows the structure to respond reversibly to the adsorption and desorption of molecules, where the materials have been found to behave both as a molecular sieve and an intercalant.[2] Discrimination of adsorbates differing in size by 0.1 Å with concomitant changes in electrical resistance of up to 10^7 Ω and fast response times have been observed, which speak well for the potential of R$_2$-Sn$_3$X$_7$ materials in chemical-sensing applications.[3,4]

The versatility of binary R$_2$Sn$_3$X$_7$ sulfide and selenide materials can be further enhanced by synthesizing ternary thioselenide isostructural analogues[5] R$_2$Sn$_3$S$_x$Se$_{7-x}$ over the entire compositional domain of $0 \leq x \leq 7$. In this way the electrical, optical, and adsorption properties of the materials can be tailored for a particular function. When a solid-state material through isomorphous compositional variations of the structure is tuned, the nature of the distribution of the elements within the structure needs to be addressed, since this can affect the properties in different ways. The main possibilities are random, ordered, segregated, and graded arrangements of the elements. In the case of close-packed structures such as the GaAl$_x$As$_{1-x}$ zinc blende lattice[6] and the SnS$_x$Se$_{2-x}$ layered berndite lattice,[7] the elements being isomorphously exchanged are distributed over a single crystallographic site. The situation is more complicated for isomorphous substitution of the open-framework structure of R$_2$Sn$_3$S$_x$Se$_{7-x}$ because the chalcogenides have the choice of being located over three crystallographically distinct sites in the lattice, comprising the μ^3-X and 3μ^2-X intracluster, and the $^6/_2\mu^2$-X intercluster bridging positions.

In this study we report details of a powder X-ray diffraction (PXRD), Fourier transform Raman (FT-Raman), ^{119}Sn cross-
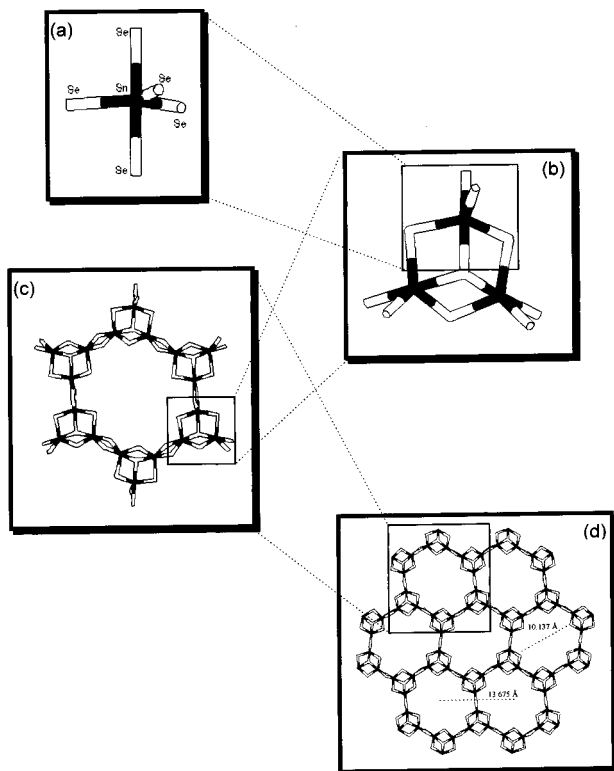
Tin(IV) Thioselenide Materials

J. Phys. Chem. B, Vol. 102, No. 13, 1998 **2357**

Figure 1. Building blocks in the structure of $TMA_2Sn_3Se_7$. (a) Distorted $SnSe_5$ trigonal-bipyramidal (TB) unit is referred to as the primary building block. (b) Connecting three TB units through a common apex and three apex−equatorial edges produces the broken-cube cluster secondary building unit. (c) A tertiary building unit is composed of six broken-cube Sn_3Se_7 clusters connected to one another through $Sn(\mu^2\text{-}Se)_2Sn$ intercluster bridges. (d) A layer of $TMA_2Sn_3Se_7$ is referred to as the quaternary building unit.

polarization magic angle spinning nuclear magnetic resonance (CP/MAS NMR), and UV−vis spectroscopy investigation of 15 isostructural ternary $TMA_2Sn_3S_xSe_{7-x}$ materials with compositions that differ by 0.5 increments of the chalcogenide over the entire range $0 \leq x \leq 7$. This particular combination of analytical techniques has revealed the nature of the chalcogenide distribution in the crystallographic unit cell at three length scales: the tertiary level of the microporous layers, the secondary level of the broken-cube clusters, and the primary building-block level of the trigonal bypyramids (Figure 1).

Experimental Section

Room-temperature PXRD patterns of all 15 samples were collected on a Siemens D-5000 diffractometer using a high-power Cu Kα X-ray source ($\lambda = 1.541\ 78$ Å) operating at 50 kV/35 mA. A Si(Li) Kevex solid-state detector was used for energy-dispersive discrimination of the Kβ component of the diffracted X-ray beam via centering of the energy window of the detector at 8.04 keV, leaving only the Cu K$\alpha_{1,2}$ lines and also enhancing the signal-to-noise ratio. The samples were ground and packed into standard sample holders, 2 mm in depth, to minimize the effect of preferred orientation of the crystallites. Strict control over sample height was maintained from sample to sample. For optimum comparison of samples all data were collected under identical running conditions with a scan step of $0.02°\ 2\theta$, 0.7 s/step within the range $6-40°\ 2\theta$, where the most informative reflections for these structures occur. A very small amount of silicon powder (−325 mesh, NBS, RSM 640-b) was mixed with the $TMA_2Sn_3S_xSe_{7-x}$ materials to serve as

an internal standard. To optimize the accuracy of the PXRD peak positions, the diffractograms used for indexing were obtained using the slow-scan mode with a step size of $0.01°\ 2\theta$ and a scan speed of 4 s/step over the range $6-40°\ 2\theta$. This is essential for achieving accurate indexing, refinement of the unit-cell parameters a, b, c, and V, and quantitative comparisons between $TMA_2Sn_3S_xSe_{7-x}$ samples.

A Bomems MB-157 Fourier transform Raman spectrometer with an InGaAs near-IR detector was used to record the FT-Raman spectra for this series. The light source is a Spectra Physics diode-pumped Nd:YLF laser emitting at 1064 nm with a 350-kHz repetition rate. Notch filters covering $150-3750$ cm^{-1} were used to discriminate against Rayleigh scattering. The instrument was configured in 180° backscattering mode. Samples were ground and then packed in sealed glass capillary tubes.

Solid-state ^{1}H/^{119}Sn CP/MAS NMR data were collected for 10 of the products on a Bruker DSX 200 spectrometer with a frequency of 74.58 MHz, recycle delay time of 5.0 s, contact time of 4 ms, 90° pulse of 3 μs, and high-power proton decoupling at 9.00 dB. Owing to the large ^{119}Sn chemical-shift anisotropy (CSA) and complications arising from the overlap of many spinning sidebands, the spectra were collected at a spinning speed of 14 kHz using the pulse program CPVA (Cross Polarization with Variable Amplitude).[8] Data were referenced to tetramethyltin, $Sn(CH_3)_4$. The number of scans was optimized for each sample in order to get a good signal-to-noise ratio and ranged from 12 000 for the end members to 34 000 for $TMA_2Sn_3S_{3.5}Se_{3.5}$, $TMA_2Sn_3S_{2.5}Se_{4.5}$, and $TMA_2Sn_{1.5}Se_{5.5}$ products. Samples were packed into 4-mm zirconium rotors. Powder X-ray diffraction studies of the samples after completing each of the NMR runs confirmed that no structural alterations had occurred during the data-acquisition period with the exception of lattice changes in the b direction (i.e., perpendicular to the planes) by about 0.1 Å due to the sensitivity of the interlayer spacing to the content of occluded water and gravitational forces.[12]

UV−visible spectra were recorded using a Varian Cary 3 double-beam spectrophotometer with a diffuse-reflectance integrating sphere. An Oriel Spectralon 99% white standard was used for background and normalization against the sample. The samples were ground and placed between two quartz disks of approximately 3-mm thickness and were placed in front of the white standard. The data were collected from 2400 to 200 nm in absorbance mode with an interval of 1 nm in order to provide enough points to achieve a statistically reasonable fit of the optical edge. An integration time of 0.68 and 0.72 s was used for the UV and NIR sections of the spectra, respectively. A scan speed of 30 nm/min and gain of 1 were used for both spectral sections with the slit mode fixed at 2.0 nm for UV and servo mode at 1.00 nm for NIR section.

Synthesis of the Materials

To study the distribution of the sulfur and selenium atoms in the structure of microporous layered tin(IV) thioselenide materials and the concomitant effect on their structural and property tuning, it was essential to obtain phase-pure products. This was achieved by optimizing the synthesis for the pure-phase orthorhombic materials through combinatorial experiments where the reaction conditions, such as the choice of precursors, concentration, temperature, heating period, mixing order, and pH, were systematically varied and established. The optimized reaction conditions summarized in Table 1 produced highly phase-pure orthorhombic $TMA_2Sn_3S_xSe_{7-x}$ (TMA^+ = tetramethylammonium cation) materials where $0 \leq x \leq 7$ with 0.5 incremental

TABLE 1: Optimized Synthesis Conditions for Pure-Phase Orthorhombic TMA$_2$Sn$_3$S$_x$Se$_{7-x}$ Materials, Where $0 \le x \le 7$, and Their Colors

reaction stoichiometry	x (moles)	y (moles)	heating period (h)	color
TMA$_2$Sn$_3$Se$_7$	0	2	20−23	dark red
TMA$_2$Sn$_3$S$_{0.5}$Se$_{6.5}$	0.14	1.86	23−25	red
TMA$_2$Sn$_3$S$_1$Se$_6$	0.29	1.71	23−27	light red
TMA$_2$Sn$_3$S$_{1.5}$Se$_{5.5}$	0.43	1.57	32−35	orange
TMA$_2$Sn$_3$S$_2$Se$_5$	0.57	1.43	39−43	orange
TMA$_2$Sn$_3$S$_{2.5}$Se$_{4.5}$	0.71	1.29	54−60	light orange
TMA$_2$Sn$_3$S$_3$Se$_4$	0.86	1.14	54−60	yellowish orange
TMA$_2$Sn$_3$S$_{3.5}$Se$_{3.5}$	1	1	57−63	yellow
TMA$_2$Sn$_3$S$_4$Se$_3$	1.14	0.86	57−63	greenish yellow
TMA$_2$Sn$_3$S$_{4.5}$Se$_{2.5}$	1.29	0.71	88−93	greenish yellow
TMA$_2$Sn$_3$S$_5$Se$_2$	1.43	0.57	88−95	green
TMA$_2$Sn$_3$S$_{5.5}$Se$_{1.5}$	1.57	0.43	93−98	light green
TMA$_2$Sn$_3$S$_6$Se$_1$	1.71	0.29	170−176	greenish blue
TMA$_2$Sn$_3$S$_{6.5}$Se$_{0.5}$	1.86	0.14	189−194	light blue
TMA$_2$Sn$_3$S$_7$	2	0	200−210	white

changes. The synthesis of this phase is dependent on the temperature, heating period, and pH of the reaction mixture.[9]

The reaction mixtures were prepared with the following stoichiometry:

$$\text{Sn:}x\text{S:}y\text{Se:TMAOH}\cdot5\text{H}_2\text{O:}33\text{H}_2\text{O}$$

where x and y are varied from 0 to 2. The reaction mixtures were prepared by initially dissolving TMAOH (tetramethylammonium hydroxide) in water in a 16-mL Enflon liner with continuous stirring. Then sulfur and/or selenium and tin metal powders were added to the reaction mixture sequentially with stirring. The mixtures were further stirred for 5 min. The liners were sealed and placed in stainless steel autoclaves and were heated at 150 °C for a specific period of time in a tumbling oven (see Table 1). The reaction mixtures were removed from the oven and allowed to cool to room temperature before the products were filtered and washed with copious amounts of water and acetone using a self-contained aspirator pump. The air-dried samples were transferred and stored in vials under an Ar atmosphere.

The reaction mixture for the TMA$_2$Sn$_3$Se$_7$ end member (denoted here on as SnSe-1 and the sulfur end member as SnS-1) gives high-quality crystals between 2 and 3 mm upon slow cooling (150 °C to room temperature over 12 h) suitable for a single-crystal X-ray diffraction study. All attempts to grow crystals of the other ternary mixtures failed to produce crystals with high enough quality for a structure determination by single-crystal X-ray diffraction.

Elemental analyses were performed at UOP, with Sn and Se determined by inductively coupled plasma (ICP) atomic absorption/emission spectroscopy and sulfur determined by ion chromatography. It was noted that the syntheses are quantitative and the number of moles of the tin and chalcogenide elements in the products are similar to that of the reactants within a 5% error margin.

Results

Powder X-ray Diffraction. Powder X-ray diffraction (PXRD) is employed as a probe of the distribution of chalcogenide atoms in the TMA$_2$Sn$_3$S$_x$Se$_{7-x}$ materials at the length scale of the unit cell. The PXRD pattern was used to fingerprint the products,
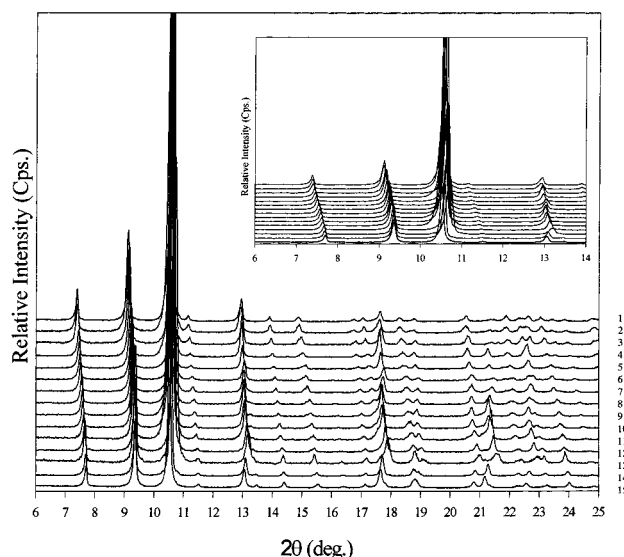
Figure 2. X-ray powder diffraction patterns for 15 members of the TMA$_2$Sn$_3$S$_x$Se$_{7-x}$ materials shown from 6 to 25° 2θ. Inset shows extended region between 6 and 14° 2θ.

to establish phase purity, to elucidate the degree of crystallinity, and to identify impurity side products and/or unreacted starting materials. In addition, the PXRD pattern is used in the indexing procedure and the determination of unit-cell parameters. Figure 2 displays the PXRD patterns of 15 TMA$_2$Sn$_3$S$_x$Se$_{7-x}$ materials, where x was varied in 0.5 increments over the entire range $0 \le x \le 7$. Inspection of the PXRD patterns establishes that the as-synthesized materials are of high purity and crystallinity. No amorphous products or unreacted materials are detected. Inspection of the diffraction patterns (Figure 2) reveals that as the selenium content of the TMA$_2$Sn$_3$S$_x$Se$_{7-x}$ materials increases, several reflections shift monotonically to lower 2θ in response to the anticipated increase in the size of the unit cell. The unit cell expands as the larger selenium atoms ($r_{cov} = 1.17$ Å) substitute for the smaller sulfur atoms ($r_{cov} = 1.04$ Å), an increase in size of 12%.[10] Note, however, that some of the PXRD reflections do not vary monotonically.

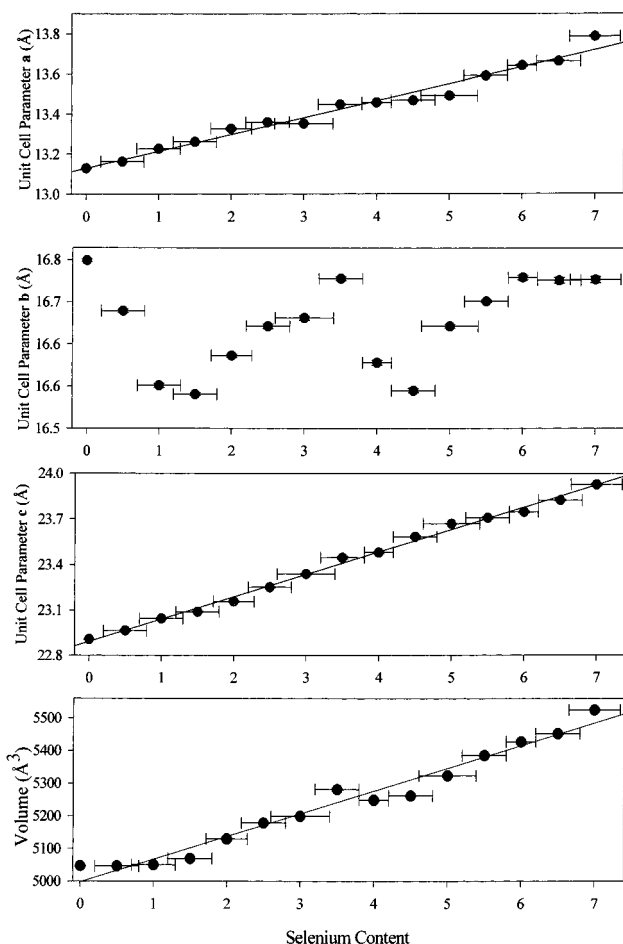The first 15−20 reflections on all diffractograms have been successfully assigned to the same orthorhombic $P2_12_12_1$ lattice as that of the TMA$_2$Sn$_3$Se$_7$ end member, confirming the isostructural nature of all samples in the entire series. The least-squares minimization program of Appleman and Evans was used to obtain the best fit between the calculated peak positions and the experimental ones.[11] All of the well-resolved reflections (N) were included in the refinement procedure of each sample where N was varied from 25 to 35 for the data presented in Table 2, which contains the calculated unit-cell parameters for the TMA$_2$Sn$_3$S$_x$Se$_{7-x}$ materials. In all cases the fit was excellent with $|\bar{\Delta}2\theta| = 0.0053-0.0163$ Å on passing from the sulfur to the selenium end member.

Figure 3 shows plots of the unit-cell parameters with respect to the selenium content of the materials (error bars are obtained from the elemental analysis). These plots show that the unit cell parameters a and c increase linearly as the selenium content increases. In contrast, the change in b parameter (see the 020 reflection at ca. 10.5° 2θ in Figure 2) is random. This nonlinear behavior is explained by the fact that the interlayer spacing in these materials is extremely sensitive to the identity and concentration of the guest molecules (e.g., water from air humidity) as well as the conditions used in sample preparation for analytical purposes. This is also evident from the change in the b parameter of a sample subjected to different pressures
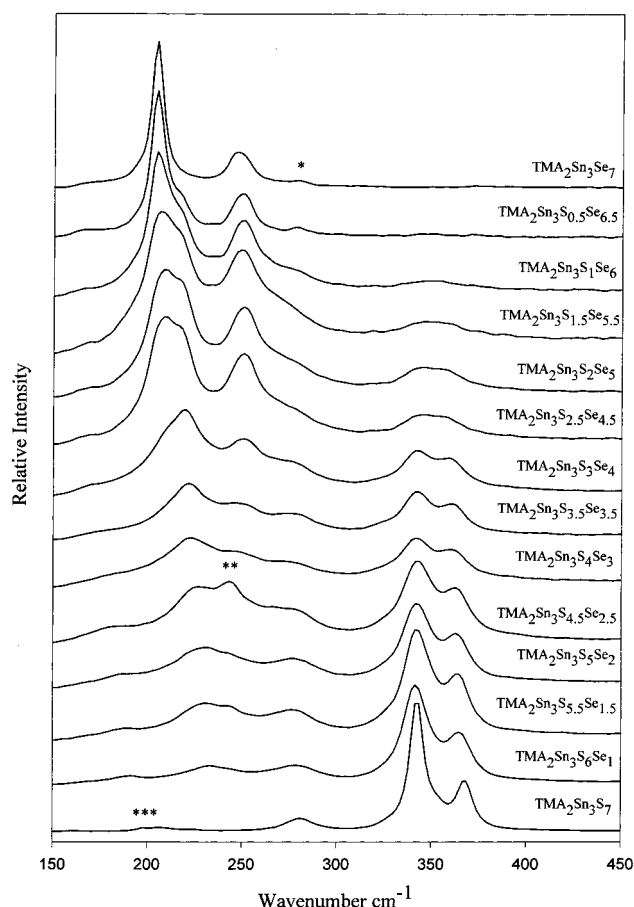
Tin(IV) Thioselenide Materials

J. Phys. Chem. B, Vol. 102, No. 13, 1998 **2359**

TABLE 2: Unit-Cell Parameters for TMA$_2$Sn$_3$S$_x$Se$_{7-x}$ Materials Obtained by Indexing Their PXRD Patterns to the Orthorhombic *P*2$_1$2$_1$2$_1$ Space Group

products[a]	a (Å)[b]	b (Å)[b]	c (Å)[b]	V (Å^3)[b]
TMA$_2$Sn$_3$Se$_7$	13.7874(40)	16.7477(50)	23.9275(78)	5525(2)
TMA$_2$Sn$_3$S$_{0.5}$Se$_{6.5}$	13.6642(36)	16.7465(47)	23.8248(58)	5452(2)
TMA$_2$Sn$_3$S$_1$Se$_6$	13.6426(62)	16.7511(40)	23.7471(62)	5427(2)
TMA$_2$Sn$_3$S$_{1.5}$Se$_{5.5}$	13.5910(40)	16.7113(23)	23.7082(74)	5385(2)
TMA$_2$Sn$_3$S$_2$Se$_5$	13.4921(81)	16.6697(31)	23.6690(19)	5323(3)
TMA$_2$Sn$_3$S$_{2.5}$Se$_{4.5}$	13.4692(39)	16.5630(35)	23.5836(80)	5261(2)
TMA$_2$Sn$_3$S$_3$Se$_4$	13.4584(41)	16.6093(40)	23.4796(71)	5248(2)
TMA$_2$Sn$_3$S$_{3.5}$Se$_{3.5}$	13.4489(29)	16.7491(30)	23.4450(83)	5281(1)
TMA$_2$Sn$_3$S$_4$Se$_3$	13.3531(47)	16.6834(36)	23.3383(50)	5199(2)
TMA$_2$Sn$_3$S$_{4.5}$Se$_{2.5}$	13.3604(41)	16.6698(37)	23.2513(41)	5178(2)
TMA$_2$Sn$_3$S$_5$Se$_2$	13.3274(59)	16.6210(27)	23.1570(59)	5129(2)
TMA$_2$Sn$_3$S$_{5.5}$Se$_{1.5}$	13.2615(38)	16.5568(25)	23.0894(51)	5069(1)
TMA$_2$Sn$_3$S$_6$Se$_1$	13.2262(31)	16.5713(34)	23.0436(45)	5050(1)
TMA$_2$Sn$_3$S$_{6.5}$Se$_{0.5}$	13.1619(20)	16.6951(28)	22.9644(49)	5046(1)
TMA$_2$Sn$_3$S$_7$	13.1289(18)	16.7792(20)	22.9077(31)	5046(9)

^{a} Nominal formula. ^{b} The numbers in parentheses show the standard deviations after the final refining cycle in the Appleman and Evans lattice cell indexing and least-squares minimization procedure. The variation in the standard deviations results from different numbers of available reflections used in the refinement procedure.

Figure 3. Plots of the unit-cell parameters a–c and the volume V vs selenium content of TMA$_2$Sn$_3$S$_x$Se$_{7-x}$ materials. Error bars refer to the selenium content.

Figure 4. FT-Raman spectra of 14 members of TMA$_2$Sn$_3$S$_x$Se$_{7-x}$, where $0 \leq x \leq 7$ with 0.5 increments: *, sulfur impurity; **, selenium impurity; ***, tin impurity.

materials is responsible for alterations in the layer spacing, layer registry, and phase transitions in these materials.[2]

The linear Vegard's law behavior of the a and c parameters suggests that the chalcogenide distribution in the layers is essentially statistical. Note that several points deviate from linearity in the plot of the unit-cell volume versus the selenium content (Figure 3) because this parameter is strongly affected by the nonlinear behavior of the b parameter. However, it does exhibit a monotonic increase, suggesting a progressive expansion of the unit cell upon introduction of selenium into the framework.

Thus, PXRD as a probe operating at the length scale of the unit cell provides evidence for a statistical distribution of chalcogenide atoms over all available sites in the lattice. The results preclude contributions from microdomains and compositional gradients where line broadening of the PXRD reflections would be expected. In addition, the evidence excludes contributions from physical mixtures of end members, since their reflections are not present in the ternary family members. Therefore, it can be concluded that on the global scale of the unit cell sensed by PXRD, the chalcogenides are statistically distributed over all crystallographically distinct sites in the lattice.

Fourier Transform Raman Spectra. Fourier transform Raman (FT-Raman) spectra of 14 samples were recorded in the range 150–3750 cm^{-1}. The spectra in Figure 4 display the framework vibrational-mode region from 150 to 500 cm^{-1}. The TMA$_2$Sn$_3$S$_{6.5}$Se$_{0.5}$ product contained a small amount of unreacted elemental selenium, and so its spectrum is not included in Figure 4. The selenium is a much stronger Raman scatterer

during grinding, the increase in the value after spinning the sample in a solid-state NMR rotor at 14 kHz, and the sensitivity of the interlayer separation and layer registry of these materials even to gravitational forces.[12] The observed nonlinearity of the interlayer spacing, as mentioned above, is very common in layered materials.[7] The change in the water content of the
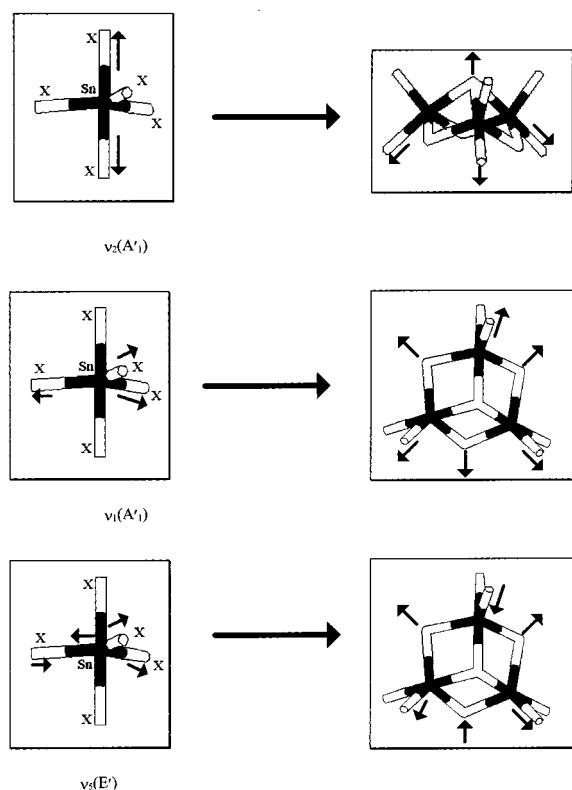
$\nu_2(A'_1)$

$\nu_1(A'_1)$

$\nu_5(E')$

Figure 5. Schematic of the normal local modes of vibration of the trigonal-bipyramidal SnX_5 unit, where X is S or Se, and correlation with related vibrational modes of the broken-cube cluster.

than the $TMA_2Sn_3S_xSe_{7-x}$ itself and produces a very intense peak at 240 cm^{-1} obstructing some of the framework modes (note that the selenium impurity is amorphous and is not detectable by PXRD). The selenium end member displays two main peaks at 202 and 248 cm^{-1} and shoulders at 195, 209, and 260 cm^{-1} corresponding to ν_{SnSe} stretching modes. The sulfide end member displays three peaks at 278, 340, and 365 cm^{-1} and shoulders at 333, 350, and 377 cm^{-1} due to ν_{SnS} stretching modes. The Raman intensity patterns from 190 to 270 cm^{-1} for the selenium end member and from 300 to 400 cm^{-1} for the sulfur end member are very similar, indicating that these two isostructural materials contain cluster and TB building blocks with comparable geometries.

Using SnX_5 (X = chalcogenide) trigonal-bipyramidal (TB) primary units to describe the structure, one can use a local-oscillator approximation to assign the FT-Raman spectra. To amplify, the observed bands can be associated with the three Raman-active $\nu_{SnS/SnSe}$ equatorial and axial stretching modes of the SnS_5 and $SnSe_5$ TBs. Figure 5 displays these three stretching modes for the trigonal-bipyramidal SnX_5 molecular building block and how they correlate with the stretching modes of the Sn_3X_7 broken-cube cluster. Thus, for the sulfide end member, the peak at 278 cm^{-1} corresponds to the totally symmetrical ν_{SnS} axial stretching mode of the TBs or the breathing mode of the capping sulfur of the broken cubes $\nu_2(A'_1)$. The peak at 340 cm^{-1} corresponds to the totally symmetrical equatorial mode $\nu_1(A'_1)$ or to the symmetrical breathing mode of the broken cubes, and the peak at 365 cm^{-1} corresponds to the asymmetrical equatorial doubly degenerate stretching mode $\nu_5(E')$ or to the asymmetrical breathing mode of the broken cubes. Comparison with a molecular analogue is useful. In molecular species such as TB $SnCl_5^-$ and $SnBr_5^-$, the three corresponding tin–halogen stretching modes are at 252, 331, 359 cm^{-1} and 154, 202, 257 cm^{-1}, respectively.[13,14] Since the Raman intensity patterns and

the peak positions of these TB molecular ions $SnCl_5^-$ and $SnBr_5^-$ are very similar to that of those of the TBs in SnS-1 and SnSe-1, respectively, it is reasonable to conclude that the lowest-frequency peak for the selenide end member is weak and must be around 165 cm^{-1} (note that 150 cm^{-1} is the cutoff of the filter used for the FT-Raman measurements). The peaks at 202 and 248 cm^{-1} belonging to the selenide end member thus correspond to equatorial symmetrical A'_1 and asymmetrical stretching E' modes, respectively.

To understand the substitution of chalcogenide atoms in the TBs, an explanation of the bonding in these systems is necessary. There are two types of bond lengths in the TB: the longer axial and the shorter equatorial ones. The σ bonding in the molecule is governed by the symmetry-allowed linear combination of the $sp^3d_{z^2}$-hybridized orbitals of the central atom with those in the equatorial and axial positions. A molecular-orbital description of the TB reveals that the axial bonds are primarily comprised of $p_zd_{z^2}$-hybridized orbitals, while the equatorial bonds are made up of sp_xp_y.[15] Greater s character of the equatorial bonds in addition to the larger overlap of the s orbitals compared to d orbitals makes the equatorial bonds stronger and shorter than the axial ones. Furthermore, the extent of the orbital overlap of the tin and chalcogenide increases with the electronegativity of the chalcogenide atoms. These two factors, in the absence of any unusual steric effects, favor the positioning of the more electronegative atom on the most weakly bound axial position. Examples of such site-selective substitution in TB molecules are well documented in the literature.[16]

By inspection of the spectra in Figure 4 and by assignment of the observed bands using TB SnS_ySe_{5-y} ($0 \leq y \leq 5$) units, it can be determined that upon substitution of selenium in TMA_2-Sn_3Se_7 by the more electronegative sulfur, the sulfur atom preferentially locates in the axial position. This is seen by the appearance and growth of the single broad peak at 278 cm^{-1} corresponding to an axial ν_{SnS} stretching mode of a TB, which becomes the capping sulfur in the cluster (Figure 5). Since an axial position in a TB of one cluster corresponds to an equatorial position of a TB in the adjacent cluster, a peak concurrently appears in the ν_{SnS} equatorial region around 350 cm^{-1}. The 350 cm^{-1} band continues to grow with increasing levels of sulfur incorporation and subsequently splits into two peaks, both components of which converge to the positions of the ν_{SnS} symmetrical and asymmetrical equatorial bands in the sulfur end member at 340 and 365 cm^{-1}, respectively. Conversely, starting with the $TMA_2Sn_3S_7$ end member and increasing the extent of selenium incorporation, one first observes the emergence of a single broad band at around 230 cm^{-1} corresponding to equatorial selenium substitution. With further selenium incorporation, this peak grows in intensity and splits into two main bands. Both components then converge as anticipated to the positions of the ν_{SnSe} symmetrical and asymmetrical equatorial bands in the selenium end member at 202 and 248 cm^{-1}. Thus, it can be seen that the spectra reveal a complementary relationship between the patterns of TB stretching modes when substituting sulfur into the selenium end member and vice versa, selenium into the sulfur end member.

The order of appearance and spectral patterns of the Raman bands on going from the selenium (top spectrum) to the sulfur end member (bottom spectrum) suggest that at the local length scale of the TBs there is preferential substitution of the axial selenium sites (consistent with this observation, note that from the bottom to top spectra in Figure 4, there is preferential substitution of the equatorial sulfur sites). This Raman-based site-selective substitution model of TBs is compatible with the
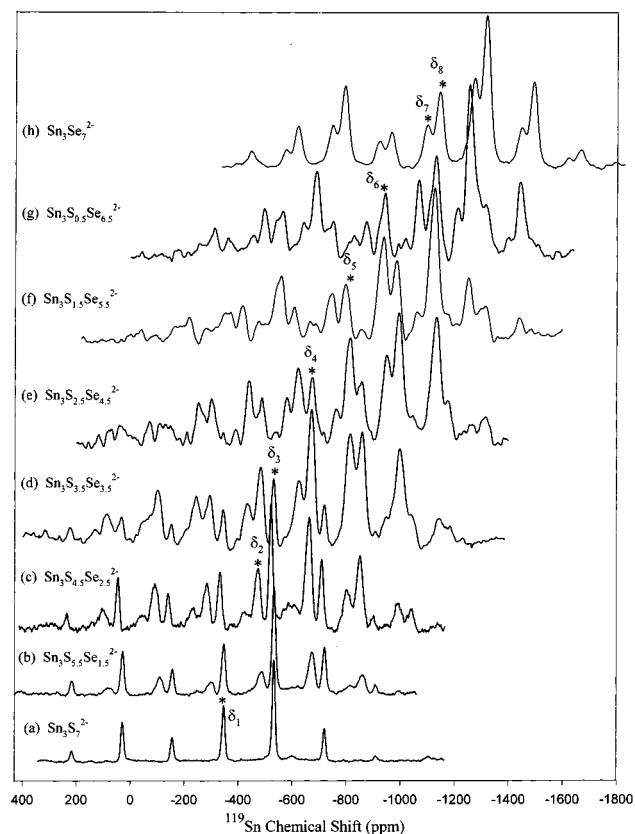
Tin(IV) Thioselenide Materials

J. Phys. Chem. B, Vol. 102, No. 13, 1998 **2361**

Figure 6. $^1H/^{119}Sn$ CP/MAS NMR spectra of $TMA_2Sn_3S_xSe_{7-x}$ materials.

PXRD picture of random substitution at the global unit-cell level, since it is reasoned that an equatorial selenium of one TB in a broken-cube cluster translates into the axial TB site of adjacent clusters. Thus, preferential chalcogenide substitution at the length scale of the TBs can naturally result in a statistical arrangement of the chalcogenides at the length scale of the clusters and hence that of the microporous layers. This model is consistent with that derived independently from solid-state NMR results presented in the next section.

^{119}Sn Solid-State CP/MAS NMR. ^{119}Sn solid-state CP/MAS NMR spectra of eight members of the $TMA_2Sn_3S_xSe_{7-x}$ materials are displayed in Figure 6. The choice of a 14-kHz spinning speed was a compromise between mechanical limits of the MAS probe and the result of numerous rotor spin rate studies aimed at determining the ^{119}Sn isotropic chemical shifts. At 14 kHz most of the isotropic chemical shifts are well separated; however, a few are hidden under the forest of spinning sidebands. Every NMR spectrum was fit using Bruker's curve-fitting program Xedplot in order to establish the isotropic chemical shift (δ_{iso}), the chemical shift anisotropy (CSA), the area under the peaks, and their full width at half-maximum (fwhm) (Table 3). The observed trends are analyzed using the SnS_ySe_{5-y} TB model with $0 \leq y \leq 5$.

^{119}Sn has a chemical shift range of more than 4500 ppm.[17] In the present samples the isotropic chemical shifts (δ_{iso}) cover a range of more than 700 ppm, thereby providing a very sensitive probe for pinpointing distinct tin chalcogenide environments. A total of eight magnetically distinct tin sites in $TMA_2Sn_3S_xSe_{7-x}$ materials are clearly identified by collecting spectra at various spinning speeds. The isotropic chemical shifts and their proposed TB site assignments are presented in Figure 7.

The $^1H/^{119}Sn$ CP/MAS NMR spectrum for the sulfur end member presented in Figure 6a consists of a series of regularly

spaced sharp peaks corresponding to a single magnetically distinct tin site with a δ_{iso} value of -345 ppm and its associated spinning sidebands. This δ_{iso} value is in agreement with the δ_{iso} for pentacoordinate tin.[18] The selenide end member however, has two isotropic chemical shifts at -1017 and -1066 ppm along with their spinning sidebands corresponding to two magnetically distinct tin sites for $SnSe_5$ TB units Figure 6h. Examination of the crystal structure of the selenide end member reveals the existence of six crystallographically distinct tin atoms in the unit cell associated with two types of broken-cube clusters. These six tin centers can be subdivided into two classes that are most likely responsible for the observation of two distinct ^{119}Sn sites in the NMR spectrum. The equatorial bond distances in all six tin centers are similar. However, in four of the TB units (type I), the axial Sn−Se bond distances are significantly longer than their equatorial counterparts. In the remaining two TBs, the axial bond lengths are significantly shorter (type II) than that in type I TBs, suggesting stronger orbital overlap in the axial direction. Ab initio calculations, by use of the STO-3G basis set and the Hartree−Fock[19,20] method, were performed using the Gaussian92[21] software package. The six distinct TB units were modeled as $SnSe_5^{5-}$ and $SnSe_5H_5$ fragments using a rigid-geometry approximation.[22] The calculations verified that there are two main types of tin center that differ with respect to the charge densities around the tin nuclei. The tin nucleus in the type II unit is less shielded owing to stronger attraction of electron density toward the axial selenium atoms, thus shifting the isotropic chemical shift to lower field ($\delta_{iso} = -1017$ ppm). Conversely, in type I units the electron density around the tin nucleus experiences less attraction toward the axial selenium atoms, resulting in a greater shielding around the tin and a shift of δ_{iso} to higher field ($\delta_{iso} = -1066$ ppm). The intensity ratio of 2:4 of the two δ_{iso} peaks, obtained from a quantitative ^{119}Sn NMR study performed without cross polarization, is consistent with the assignment of the observed isotropic chemical shifts to two crystallographically and magnetically distinct tin sites in the selenide end member.[22] These sites are not resolved in the less distorted sulfur end member (see below).

The breadth of the peaks observed in the $^1H/^{119}Sn$ CP/MAS NMR spectra for the selenium end member is greater than that observed for the peaks of the sulfur analogue. The peak broadening can be attributed to a more distorted geometry of the $SnSe_5$ TB units. This could be due to the longer Sn−Se bond lengths and weaker bond strengths, allowing enhanced flexibility of the framework and larger angular distortions around TB and cluster building units (see discussion of CSA below).

As the selenium content in the $TMA_2Sn_3S_xSe_{7-x}$ materials increases, peaks corresponding to new tin sites arise (Figure 6). These new peaks first emerge with a low intensity and reach a maximum intensity with narrow line widths before they decay to zero. The isotropic chemical shift values monotonically advance to higher field upon substitution with selenium (note that the less electronegative selenium shields the tin nucleus more than sulfur). Initially, the selenium is preferentially substituted into the equatorial position of SnS_5 TB units to produce SnS_4Se, creating a new peak at $\delta_{iso} = -486$ ppm (structure (2) in Figure 7). The intensity of the peak gradually increases to a maximum and slowly disappears. Two peaks appear in unison after $TMA_2Sn_3S_{5.5}Se_{1.5}$, (Figure 6b), which relate to two different yet expected geometries for the SnS_3Se_2 unit. The peak at $\delta_{iso} = -531$ ppm (note that, at a spinning rate of 14 kHz this peak is superimposed on the first spinning sideband of δ_1) has been assigned to the SnS_3Se_2 unit with one selenium atom in the equatorial and one in the axial position

TABLE 3: Results of the NMR Spectral Analysis of Eight Members of the Family of TMA$_2$Sn$_3$S$_x$Se$_{7-x}$ Materials[a]

no.	product	site	δ_{iso} (ppm)	fwhm (ppm)	% peak area	shielding anisotropy $\Delta\sigma$ (ppm)	σ_{11} (ppm)	σ_{22} (ppm)	σ_{33} (ppm)
1	TMA$_2$Sn$_3$S$_7$	1	−345	13.6	100	1005 ± 25	−682	−682	323
2	TMA$_2$Sn$_3$S$_{5.5}$Se$_{1.5}$	1	−345	17.5	45.3	1096 ± 27	−784	−638	385
		2	−486	31.1	23.8	955 ± 29	−883	−723	152
		3	−531	17.4	9.2				
		4	−673	31.1	12.0				
		5	−813	34.1	9.5				
3	TMA$_2$Sn$_3$S$_{4.5}$Se$_{2.5}$	1	−345	28.6	25.8	1169 ± 28	−737	−737	432
		2	−486	37.6	32.7	1112 ± 32	−1100	−618	253
		3	−531	28.8	13.2				
		4	−673	32.7	16.6				
		5	−813	30.2	11.7				
4	TMA$_2$Sn$_3$S$_{3.5}$Se$_{3.5}$	2	−486	29.7	17.5				
		3	−531	19.2	10.5				
		4	−673	33.1	32.6	715 ± 42	−1147	−670	−194
		5	−813	40.0	32.7	743 ± 45	−1261	−864	−319
		6	−948	33.3	6.7	801 ± 49	−1345	−1104	−424
5	TMA$_2$Sn$_3$S$_{2.5}$Se$_{4.5}$	2	−486	34.2	12.4				
		3	−530	15.8	6.6				
		4	−673	41.6	21.7	846 ± 49	−1219	−683	−105
		5	−813	41.6	32.9	872 ± 50	−1260	−941	−229
		6	−947	41.0	26.4	928 ± 56	−1259	−1259	−331
6	TMA$_2$Sn$_3$S$_{1.5}$Se$_{5.5}$	4	−673	19.0	7.8				
		5	−813	20.3	11.8	946 ± 47	−1267	−952	−164
		6	−947	33.7	55.2	933 ± 47	−1248	−1248	−315
		7	−1017	10.9	1.2				
		8	−1065	30.6	23.9	1202 ± 60	−1462	−1462	−260
7	TMA$_2$Sn$_3$S$_{0.5}$Se$_{6.5}$	5	−813	33.5	5.4				
		6	−947	26.3	33.8	1023 ± 46	−1350	−1214	−259
		7	−1017	25.9	12.4				
		8	−1066	31.1	48.3	1194 ± 53	−1525	−1405	−271
8	TMA$_2$Sn$_3$Se$_7$	7	−1017	35.6	32.0	1152 ± 46	−1441	−1364	−250
		8	−1066	33.6	68.0	1208 ± 48	−1611	−1329	−262

[a] The CSA values that are left blank are due to the low intensity of the peaks in the spectrum and poor signal-to-noise ratio, making them difficult to analyze. ESDs: $\delta_{iso} = \pm 2$.
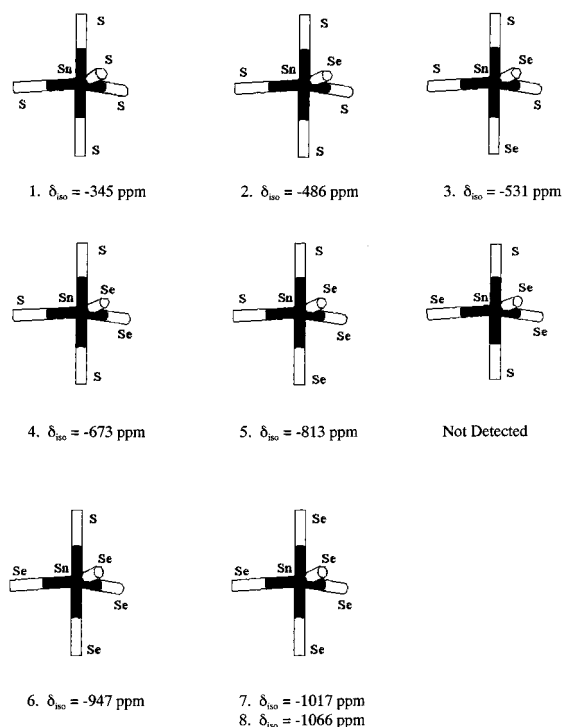

1. δ_{iso} = -345 ppm   2. δ_{iso} = -486 ppm   3. δ_{iso} = -531 ppm

4. δ_{iso} = -673 ppm   5. δ_{iso} = -813 ppm   Not Detected

6. δ_{iso} = -947 ppm   7. δ_{iso} = -1017 ppm   8. δ_{iso} = -1066 ppm

Figure 7. Proposed structural models of SnS$_y$Se$_{5-y}$ trigonal-bipyramidal building units, where $0 \leq y \leq 5$, with their corresponding ^{119}Sn NMR isotropic chemical shifts.

((3) of Figure 7), and the $\delta_{iso} = -673$ ppm peak has been assigned to the SnS$_3$Se$_2$ unit, with two selenium atoms located

in the equatorial position ((4) of Figure 7). This assignment is based on the fact that there is more s-orbital character in the equatorial site of the TB. Furthermore, the more electronegative equatorial sulfur atom leaves the tin center with less s-electron density, thus deshielding the nucleus. These arguments support the assignment made for these two sites. In TMA$_2$Sn$_3$S$_{4.5}$Se$_{2.5}$ (Figure 6c), the fifth site is also observed at $\delta_{iso} = -813$ ppm, which is associated with SnS$_2$Se$_3$ having two equatorial and one axial selenium, as shown in (5) of Figure 7. In TMA$_2$-Sn$_3$S$_{3.5}$Se$_{3.5}$ (Figure 6d), the sixth site appears for the first time at $\delta_{iso} = -947$ ppm, which relates to SnSSe$_4$ with three equatorial and one axial selenium ((6) of Figure 7). Finally, peaks 7 and 8 emerge simultaneously after the TMA$_3$Sn$_3$S$_{1.5}$-Se$_{5.5}$ product (Figure 6f) and become the only peaks in the selenium end member (Figure 6h). No peaks could be detected for the SnS$_{(ax)2}$Se$_{(eq)3}$ site (Figure 7 (not detected)) perhaps because of either peak overlap or a low population in the sample. As shown in Figure 8, there is a linear relationship between the δ_{iso} values and the selenium content of the TB units as the number of Se atoms increase from zero to five in SnS$_y$Se$_{5-y}$ but with a notable discontinuity between sites 3 and 4. The deshielding effect of the equatorial S in site 3 changes to a shielding effect of the equatorial Se in site 4 and is considered likely to be the cause of the break in the curve shown in Figure 8.

The CSA values determined for members of the TMA$_2$Sn$_3$S$_x$Se$_{7-x}$ family of materials are listed in Table 3. Certain interesting trends in the CSA become apparent, such as an overall increase on passing from the sulfide to selenide end member, which implies a decrease in the symmetry of the
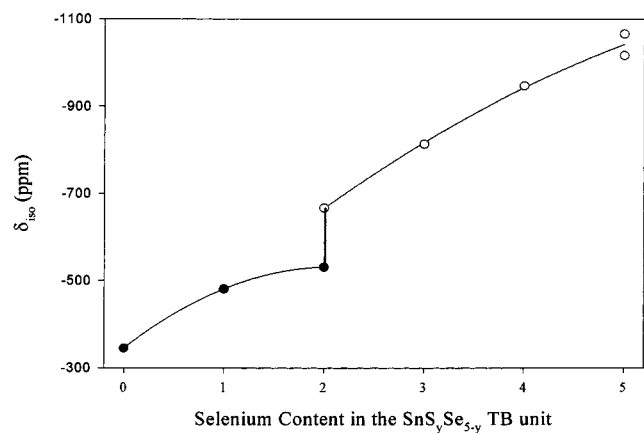
Tin(IV) Thioselenide Materials

J. Phys. Chem. B, Vol. 102, No. 13, 1998 **2363**

Figure 8. Plot of the ^{119}Sn NMR isotropic chemical shift vs the number of selenium atoms in the SnS_ySe_{5-y} TB units, where $0 \leq y \leq 5$.

Figure 9. Distribution of SnS_ySe_{5-y} TB units, where $0 \leq y \leq 5$, vs the selenium content of $TMA_2Sn_3S_xSe_{7-x}$ products as determined by ^{1}H/^{119}Sn CP/MAS NMR: (1) $SnS_{(ax)2(eq)3}$; (2) $SnS_{(ax)2(eq)2}Se_{(eq)}$; (3) $SnS_{(ax)(eq)2}Se_{(ax)(eq)}$; (4) $SnS_{(ax)2(eq)}Se_{(eq)2}$; (5) $SnS_{(ax)(eq)}Se_{(ax)(eq)2}$; (6) $SnS_{(ax)}Se_{(ax)(eq)3}$; (7) $SnSe_{(ax)2(eq)3}$. The normalized intensities are plotted for each site in each spectrum.

electronic environment around the tin nucleus. The axial line shape of the sulfide end member transforms to orthorhombic in the selenide analogue. Also, the line shape becomes orthorhombic as soon as the first Se is introduced in the sulfide framework. Both magnetically distinct sites in the selenide end member have orthorhombic line shapes. All of this points to an increasingly distorted geometry around the TB tin sites in the selenium-rich materials, as proposed above based on chemical-shift arguments. It is noteworthy that the CSA corresponding to the $\delta_{iso} = -1017$ ppm tin selenide center is smaller than the one corresponding to $\delta_{iso} = -1066$ ppm. This is consistent with the proposal that the $SnSe_5$ TB unit with the shorter axial bonds creates a more symmetrical electron distribution around the tin nucleus. Another interesting point concerns the observation that δ_{iso} is found to be essentially invariant for a particular TB tin site in $TMA_2Sn_3S_xSe_{7-x}$ for different values of x; however, there does exist considerable variability in the respective chemical-shift tensor components and CSA. This implies that while δ_{iso} reflects the local electron density around a tin center in the framework, the CSA senses the symmetry of the electron distribution beyond the TB and may in fact extend to the length scale of the broken-cube clusters or even the microporous layers themselves.

Figure 9 displays the variation in peak areas for seven distinct TB tin sites for the above-mentioned 10 samples. This plot quantitatively depicts the distribution of the different tin TB environments with respect to the selenium content in the framework. Although the selenium concentration dependence of the population of TB tin sites in $TMA_2Sn_3S_xSe_{7-x}$ is clearly not strictly binomial, the pattern of their growth and decay does suggest that statistical effects of some kind are contributing to the chalcogenide distribution in the framework. Earlier work from this laboratory has shown that the $[Sn_2S_6]^{4-}$ dimer is the fundamental solution-phase building block that is responsible for the template-directed assembly of the microporous layered framework in $TMA_2Sn_3S_7$. The structure of the D_{2d} symmetry dimer is comprised of two SnS_4 tetrahedral units connected on a common edge, $[S_2Sn(\mu\text{-}S)_2SnS_2]^{4-}$. Two of these dimers snap together to create the broken-cube cluster that subsequently organizes into chains and sheets to create the parallel stacked microporous layers in $TMA_2Sn_3S_7$.[22,23]

Interestingly, the availability of the data shown in Figure 9 allows one to uniquely elaborate upon the proposed reaction pathway for the templated self-assembly of the $TMA_2Sn_3S_7$ framework.[22] The sulfur and selenium distribution in the framework provides information akin to an isotope-substitution experiment and in principle can unveil information on the details
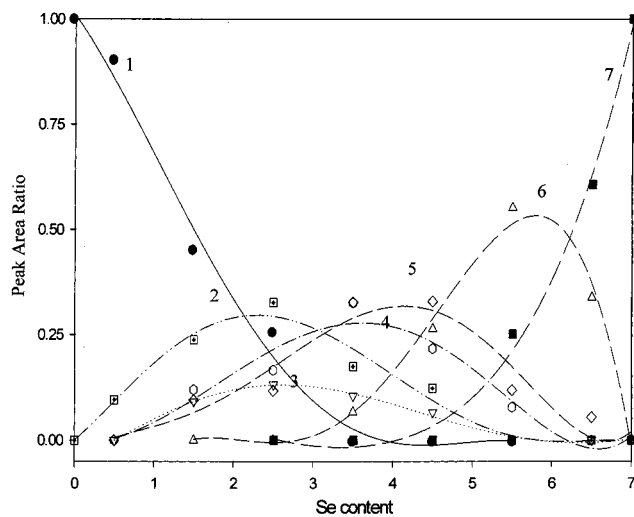
of the self-assembly pathway.[22] In this context, work from this laboratory has shown that in germanium thioselenide adamantanoid clusters, the less electronegative selenium prefers to occupy terminal rather than bridging sites. With this as a precedent for site-selective substitution, a self-assembly scheme can be formulated for $TMA_2Sn_3S_xSe_{7-x}$ that involves the unison of tin thioselenide dimers to form the broken-cube clusters, with the restriction that terminal sites of the dimer will be selectively substituted by selenium. The results of this purely statistical approach for the distribution of TB tin sites turn out to be very close to the observed distribution (Figure 9). The inclusion of isomers such as gem-$[Se_2Sn(\mu^2\text{-}S)_2SnS_2]$,[4-] cis-$[SSeSn(\mu^2\text{-}S)_2$-$SnSSe]^{4-}$, and $trans$-$[SSeSn(\mu^2\text{-}S)_2SnSSe]^{4-}$ has very little effect on the distribution shown in Figure 9. As a control calculation, the assembly was repeated with the opposite assumption, namely, that the selenium prefers to substitute into the bridging positions of the dimer. The results of this assembly pathway, however, has very little similarity to the observed distribution. One may conclude from this simple analysis that the observed chalcogenide distribution in the $TMA_2Sn_3S_xSe_{7-x}$ family of materials, as determined by ^{1}H/^{119}Sn CP/MAS NMR, is consistent with a dimer-based reaction scheme in which terminal selenium substitution is favored in the precursor dimer units that assemble into the framework and that equatorial selenium is preferred in the TB building blocks that constitute the 2,2,3-connected two-dimensional network.[22,23]

Diffuse-Reflectance UV−Visible Spectroscopy. The $TMA_2Sn_3S_xSe_{7-x}$ materials, which are perceived to have numerous advanced material applications,[2,5,12] are the open-framework analogues of the layered bulk semiconductors SnS_xSe_{2-x}.[24,25] Determination of the chalcogenide dependence of optical band gaps of the $TMA_2Sn_3S_xSe_{7-x}$ family members provides information regarding the tunability of the energy separation between the valence band (VB) and the conduction band (CB), thereby, bringing to practice the concept of band-gap engineering of the properties of these materials.

Diffuse-reflectance spectra of 15 samples of the $TMA_2Sn_3S_xSe_{7-x}$ series are displayed in Figure 10. Each spectrum was normalized with respect to the low-energy band. The absorption edge monotonically red-shifts as the selenium content increases in the framework of the materials, giving each
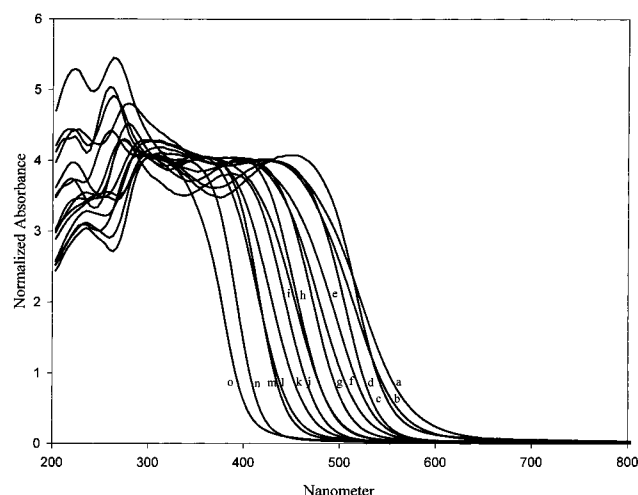
2364 *J. Phys. Chem. B, Vol. 102, No. 13, 1998*

Ahari et al.

Figure 10. Compositional dependence of the optical reflectance spectra of $TMA_2Sn_3S_xSe_{7-x}$ materials: (a) $TMA_2Sn_3Se_7$; (b) $TMA_2Sn_3S_{0.5}Se_{6.5}$; (c) $TMA_2Sn_3S_1Se_6$; (d) $TMA_2Sn_3S_{1.5}Se_{5.5}$; (e) $TMA_2Sn_3S_2Se_5$; (f) $TMA_2Sn_3S_{2.5}Se_{4.5}$; (g) $TMA_2Sn_3S_3Se_4$; (h) $TMA_2Sn_3S_{3.5}Se_{3.5}$; (i) $TMA_2Sn_3S_4Se_3$; (j) $TMA_2Sn_3S_{4.5}Se_{2.5}$; (k) $TMA_2Sn_3S_5Se_2$; (l) $TMA_2Sn_3S_{5.5}Se_{1.5}$; (m) $TMA_2Sn_3S_6Se_1$; (n) $TMA_2Sn_3S_{6.5}Se_{0.5}$; (o) $TMA_2Sn_3S_7$.

sample a characteristic color (see Table 1). In addition, the optical band edges of these materials are blue-shifted by about 0.9 eV with respect to their bulk SnS_xSe_{2-x} analogue materials. To calculate the optical band gap of these materials, reflectance was transformed to absorbance data using the Kubelka–Munk method.[26]

The absorption edge for the bulk SnS_xSe_{2-x} type materials has been determined to arise from indirect electronic transitions.[27–29] It was, however, established in another study that the sulfur end member SnS-1 displays luminescence with a lifetime in the range 20–200 ns, suggesting that the material is electronically direct.[12] Thus, the band edges were fit to the quantum-mechanical expression for a direct allowed (da) interband electronic transition according to

$$\alpha_{da} = C_{da}(\hbar\omega - E_g)^{1/2}$$

where α_{da} is the absorption coefficient, C_{da} is a coefficient with little energy dependence, $\hbar\omega$ is the photon energy, and E_g is the optical band gap.[29] The optical band gap was determined using a Mathcad program by first plotting the spectra to $\alpha_{da}{}^2$ as a function of energy $\hbar\omega$ and then measuring the intersection of a line passing through the optical edge and its intersection with the energy axis to yield E_g.

The correlation of the optical band gaps with the selenium content fits best to a polynomial function showing a fairly steep decay of E_g on increasing the selenium content up to the $TMA_2Sn_3S_3Se_4$ product, after which point the decay reaches a plateau and does not further change much (Figure 11). The smaller slope of the fitted curve at the low-energy and high selenium section of the plot in Figure 11 could arise from the changeover from a mainly localized electronic structure for SnS-1 to a more delocalized one for SnSe-1. It suggests that after the TMA_2-$Sn_3S_3Se_4$ product, the selenium-substituted broken cubes begin to percolate throughout the microporous layers, thereby changing the electronic band properties of the framework from a localized to a delocalized description. This is a type of insulator–semiconductor transition. Another possible explanation of the behavior in Figure 11 involves the electronic coupling of selenium-rich broken-cube clusters to create islands that increase in size with selenium content, causing the absorption edge to
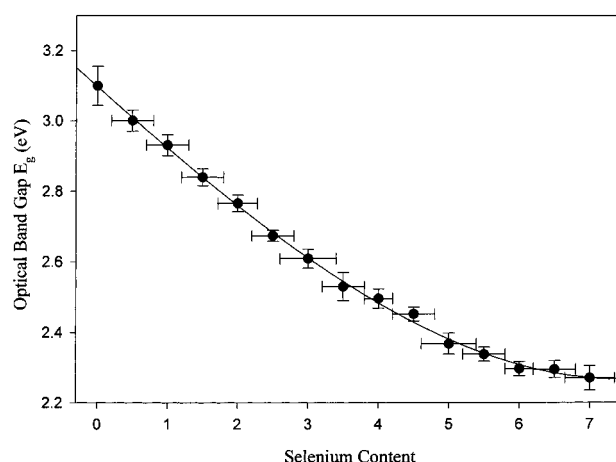

Figure 11. Plot of measured optical band gap E_g (eV) of $TMA_2Sn_3S_xSe_{7-x}$ vs selenium content of the materials.

red-shift. Recall that quantum size effects (QSEs) in semiconductor nanostructures (i.e., quantum wells, wires, and dots) are responsible for the commonly observed size-dependent shifting of the optical band edge.[30] Charge-transport studies are underway to further explore the origin of the selenium concentration dependence of the optical band gaps in the $TMA_2Sn_3S_xSe_{7-x}$ family of materials.[31]

Discussion

Inspection of the experimental results for the chalcogenide compositional dependence of the dimensions of the unit-cell (Figure 3), energies of the optical band-gap (Figure 11), vibrational frequencies of the Sn–S/Se skeletal stretching modes (Figure 4), and ^{119}Sn NMR isotropic chemical shifts (Figure 8) for the series of 15 isostructural ternary $TMA_2Sn_3S_xSe_{7-x}$ materials unveils some interesting trends. Three types of chalcogenide effect can be identified: first, linear Vegard's law behavior of the dimensions of the porous layers over the entire composition range, seen by PXRD; second, linear behavior with discontinuities in the NMR chemical-shift behavior and FT-Raman spectral changes; third, nonlinear negative Vegard's Law behavior for the optical band-gap energies. The results imply that the diffraction and spectroscopy techniques employed are interrogating the microporous layered $TMA_2Sn_3S_xSe_{7-x}$ structure at three distinct length scales. Here, the differences in the composition behavior of measured physical properties are revealing aspects of the chalcogenide distribution at the level of the crystallographic unit cell, the broken-cube clusters, and the TBs. Recollect that Vegard's law is an empirical expression used to describe the observation that the compositional variation of the physical properties of a ternary solid usually emerges as the atomic weighted fraction of the respective properties of the two binary end members.[32]

To emphasize, the PXRD results appear to be reporting on how the chalcogenide composition globally influences the dimensions of the layers and their packing into the primitive unit cell. The observation, over the entire compositional domain, of strictly linear Vegard's law behavior of the intralayer dimensions implies that for this particular physical property and length scale, the material is responding to composition variations as if the chalcogenides are randomly distributed. At this level, PXRD does not distinguish between TBs or broken-cube clusters. This does not, however, appear to be the case for the spectroscopic results. The chalcogenide effect on the $\nu_{SnS/Se}$ skeletal frequencies and [119]Sn isotropic chemical shifts is seen to be best described with TBs, while the optical band gaps fit

better to a nonlinear negative-type Vegard's law. This difference in behavior suggests that a local description at the level of the TB primary building block more accurately describes the FT-Raman and NMR data, whereas the cluster secondary building level is more appropriate for analyzing the optical-absorption results.

To expand upon this proposal, consider first the ^{1}H/^{119}Sn CP MAS NMR data, which unveil the existence of eight magnetically distinct sites in the lattice of TMA$_2$Sn$_3$S$_x$Se$_{7-x}$. There are several noteworthy trends in the data. To begin, the isotropic chemical shift moves to higher field with increasing selenium content. This is expected as the more electropositive selenium magnetically shields the tin nucleus to a greater extent than the sulfur. The chalcogenide compositional dependence of the chemical shift shows a linear trend with a break upon incorporation of two Se into TBs where there coexist two possible configurations at the discontinuity (see Figure 8). Recall that the isotropic chemical shift reflects the local distribution of electronic charge around the NMR-active nucleus. Therefore, the observation of eight distinct tin environments provides compelling evidence for a local description of chalcogenide site preferences in the lattice.

The most reasonable explanation for this phenomenon has, as a basis, the most energetically favored arrangement of chalcogenides in the TB SnS$_y$Se$_{5-y}$ primary building block for the range $0 \leq y \leq 5$. The larger percentage of d$_{z^2}$-orbital character in the axial and s-orbital character in the equatorial positions makes the orbital overlap for the equatorial bonds greater than that of the axial ones, which results in stronger and shorter equatorial bonds in TBs. This difference in overlap properties between the equatorial and axial sites is the origin of site preferences in ternary TBs. Numerous examples of this have been reported[15,16] and reveal a propensity for the most electronegative atom to occupy the axial site positions. Because orbital overlap scales with electronegativity, the energetically most stable stereochemistry for ternary TBs locates the most strongly bound atom in the most weakly bound site.

This idea underpins the observation of site preferences of the chalcogenides in the TB SnS$_y$Se$_{5-y}$ building blocks of the TMA$_2$Sn$_3$S$_x$Se$_{7-x}$ structure and provides a natural explanation for the observation of eight ^{119}Sn lattice sites, with two distinct regions, for the composition dependence of NMR chemical shifts. Beginning with the TMA$_2$Sn$_3$S$_7$ end member, the first selenium to isomorphously substitute into the structure is expected to enter the equatorial TB site. Note that the three intercluster Sn(μ^2-Se)$_2$Sn bridge bonds each contain one TB equatorial and one axial site and therefore contribute 1.5 Se to the total count of 4.5 equatorial sites.

Also, an intercluster Sn(μ^2-Se)Sn bridge bond that originates in an equatorial TB on one cluster is axial on the adjoining cluster. This is the likely explanation for the detection of eight rather than nine distinct tin sites (note that the site, where all the Se atoms are in the equatorial position and all the sulfur atoms are in the axial position, is not observed). Since the orbital overlap is less for the axial compared to the equatorial bonds, it is reasonable to observe the ^{119}Sn NMR signal of site 4 at higher field than site 3 (see Figure 7) (note that these two sites have the same number of Se atoms in the TB units and site 4 likely has more s-electron density around the tin nucleus). Thus, the chalcogenide dependence of the NMR chemical shifts in TMA$_2$Sn$_3$S$_x$Se$_{7-x}$ probes the valence-electron distribution at the length scale of the smallest building unit, namely, the TB SnS$_y$Se$_{5-y}$. Even though equatorial substitution of sulfur by selenium in the TBs is preceded by axial substitution, the

chalcogenide distribution remains statistical and closely follows Vegard's law (PXRD results).

The observed trend in the composition dependence of the Raman $\nu_{SnS/Se}$ skeletal frequencies of the TMA$_2$Sn$_3$S$_x$Se$_{7-x}$ series resembles that of the isotropic NMR chemical shifts. This implies that the Raman effect interrogates the local modes of the TB SnS$_y$Se$_{5-y}$ building units and defines equatorial-site preferences for selenium as described earlier. By comparison with the Raman assignments of the skeletal stretching modes for the similar mass molecular species SnCl$_5^-$ and SnBr$_5^-$, the three predominant Raman bands observed for the end members TMA$_2$Sn$_3$S$_7$ and TMA$_2$Sn$_3$Se$_7$ can be assigned, in order of decreasing frequency, to the E$'$ and A$_1'$ equatorial modes and A$_1'$ axial mode. Through cross-correlation of the order of appearance of the eight TB SnS$_y$Se$_{5-y}$ sites detected in the NMR spectra with bands showing up in the Raman spectra, it is found that equatorial precedes axial substitution of sulfur by selenium in TMA$_2$Sn$_3$S$_7$ and conversely that axial precedes equatorial substitution of selenium by sulfur atoms in TMA$_2$Sn$_3$Se$_7$.

The absorption edge of the TMA$_2$Sn$_3$S$_x$Se$_{7-x}$ series monotonically shifts to lower energies with increasing selenium content. Knowing from luminescent-lifetime measurements[12] that TMA$_2$Sn$_3$S$_7$ is best described as a direct band-gap electronic material, the chalcogenide composition dependence of the VB-to-CB energy can be estimated for each of the 15 samples by fitting the absorption edge to the quantum-mechanical expression for direct interband transitions.[29] The optical band gaps calculated in this way fit best to a nonlinear negative Vegard's law. In terms of the valence-orbital ionization potentials and orbital overlaps of the chalcogenide relative to tin, the VB$-$CB band-gap energy is expected to diminish with selenium content. This change is reflected in the measured electrical conductivities of the TMA$_2$Sn$_3$S$_7$ and TMA$_2$Sn$_3$Se$_7$ end members.[31] Thus, it is reasonable to assume, that as the selenium content increases in the TMA$_2$Sn$_3$S$_x$Se$_{7-x}$ series, a transition takes place from a localized electronic description in terms of TBs to a delocalized band picture in which the clusters become electronically coupled. This alteration in electronic character from "bonds to bands"[33] is most likely responsible for the observation of nonlinear negative Vegard's law behavior where the most dramatic change in the rate of decrease of the optical band gap occurs around a S/Se ratio of 3:4, possibly denoting an insulator$-$semiconductor transition in the framework of TMA$_2$Sn$_3$S$_x$Se$_{7-x}$. This is expected to occur when the population of intercluster Sn(μ^2-Se)Sn bridge bonds reaches the percolation limit, thereby permitting delocalization of electronic charge density throughout the microporous layered structure. It is likely that a minimum of two Sn(μ^2-Se)Sn intra- and intercluster bridge bonds per cluster will facilitate efficient electronic coupling over two spatial dimensions, and therefore, percolation should emerge after introducing about three selenium atoms into the TMA$_2$Sn$_3$S$_x$Se$_{7-x}$ structure.

Conclusions

The TMA$_2$Sn$_3$S$_x$Se$_{7-x}$ family of tin thioselenide materials can be considered to be structural analogues of bulk SnS$_x$Se$_{2-x}$ semiconductors, where microporous layers comprise the former and where dense layers make up the latter. The structural, physical, and chemical properties of both classes of materials can be finely tuned by systematic variations of the chalcogenide composition. In the case of SnS$_x$Se$_{2-x}$ the chalcogenides are distributed over a single type of crystallographic site in densely packed layers. By contrast, the chalcogenides in TMA$_2$Sn$_3$S$_x$Se$_{7-x}$ are distributed over three crystallographically distinct sites in

2366 *J. Phys. Chem. B, Vol. 102, No. 13, 1998*

Ahari et al.

layers that are close-packed with a honeycomb arrangement of micropores. Although the chalcogenides are randomly distributed within the layers of SnS_xSe_{2-x} and the physical properties of the materials display linear Vegard's law behavior, the situation in $TMA_2Sn_3S_xSe_{7-x}$ is more subtle and the chalcogenide arrangement and physical properties need to be explored at different length scales. This is achieved by combining the results obtained from PXRD, optical, vibrational, and NMR spectroscopy. The chalcogenide dependence of the PXRD-determined unit-cell parameters shows that the dimensions of the microporous layers follow a linear Vegard's law. By contrast, at the length scale of the SnS_ySe_{5-y} TB primary building blocks, ^{119}Sn NMR and FT-Raman spectroscopy establish that the chalcogenide distribution is not statistical because of selenium site preferences for equatorial substitution. Because certain axial and equatorial bonds in the TBs can form bridges between the broken-cube cluster secondary building blocks, the chalcogenide dependence of the optical band-gap energies displays nonlinear negative Vegard's law behavior.

The overall picture that emerges from this study is that although Raman vibrational frequencies and ^{119}Sn NMR isotropic chemical shifts recognize the local electron density around the tin centers, the NMR chemical-shift anisotropy and optical band gaps sense the symmetry and the extent of the electron distribution beyond the TBs. This may extend to the length scale of the broken-cube clusters and further to the structure of the microporous layers, as defined by PXRD. Last, and by no means least, the NMR-defined chalcogenide distribution in $TMA_2Sn_3S_xSe_{7-x}$ provides an unprecedented detailed insight into the $[Sn_2S_6]^{4-}$ self-assembly pathway to the $TMA_2Sn_3S_7$ material.[23] The work reported in this study is considered to represent a significant step toward the development of compositionally tailorable microporous semiconductors, molecule-discriminating chemical sensors, and electrically tunable membranes.[2,3,31]

References and Notes

(1) Bowes, C. L.; Ozin, G. A. *Adv. Mater.* **1996**, *8*, 13. Sheldrick, W. S.; Wachhold, M. *Angew. Chem., Int. Engl.* **1997**, *36*, 206. Kanatzidis, M. G. *Chem. Mater.* **1990**, *2*, 253. Bowes, C. L. Ph.D. Thesis, University of Toronto, 1996. Jiang, T. Ph.D. Thesis, University of Toronto, 1997. Francis, R. J.; Price, S. J.; Evans, J. S.; O'Brien, O. S.; O'Hare, D.; Clark, S. M. *Chem. Mater.* **1996**, *8*, 2102.

(2) Ozin, G. A. *Supramol. Chem.* **1995**, *6*, 125. Ozin, G. A.; Bowes, C. L.; Jiang, T.; Lough, A. J.; Petrov, S.; Vovk, G.; Verma, A.; Young, D. Electrical Sieves for Molecular Recognition. In *Proceedings of the 9th International Symposium on Molecular Recognition and Inclusion*; Coleman, A., Eds.; Kluwer Academic: Dordrecht, The Nederlands, 1997.

(3) Ozin, G. A. *Adv. Mater.* **1992**, *4*, 612.

(4) Bedard, R. L.; Vail, L. D.; Wilson, S. T.; Flanigen, E. M. U.S. Patent 4,880,761, 1989.

(5) Ahari, H.; Bedard, R. L.; Ozin, G. A.; Petrov, S.; Young, D. *Adv. Mater.* **1995**, *7*, 370.

(6) Reed, M. A.; Bate, R. T.; Bradshaw, K.; Duncan, W. M.; Frensley, W. R.; Lee, J. W.; Shih, H. D. *J. Vac. Sci. Technol.* **1986**, *B4*, 358.

(7) Rimmington, H. P. B.; Balchin, A. A.; Tanner, B. K. *J. Cryst. Growth* **1972**, *15*, 51. Rimmington, H. P. B.; Balchin, A. A. *Phys. Status Solidi A* **1971**, *6*, K47. Boudjouk, P.; Seidler, D.; Grier, D.; McCarthy, G. *J. Chem. Mater.* **1996**, *8*, 1189.

(8) Smith, S. O.; Kustanovich, I.; Wu, X.; Peersen, O. B. *J. Magn. Reson. Ser. A* **1993**, *104*, 334.

(9) Ahari, H. Ph.D. Thesis, University of Toronto, 1998.

(10) Emsley, J. *The Elements*, 2nd ed.; Clarendon Press: Oxford, 1991.

(11) Appleman, D. E.; Evans, H. T., Jr. 1973, USGS-GD-73-003, Report 2D, (revised by Benoit, P. H.), PC version 3.1; National Technical Information Service, Document PB2-16188, 1987.

(12) Ahari, H.; Bedard, R. L.; Bowes, C. L.; Coombs, N.; Dag, Ö.; Jiang, T.; Ozin, G. A.; Petrov, S.; Sokolov, I.; Verma, A.; Young, D. *Nature* **1997**, *388*, 857. Dag, Ö.; Ahari, H.; Coombs, N.; Jiang, T.; Aroca-Ouellette, P.; Petrov, S.; Sokolov, I.; Verma, A.; Vovk, G.; Young, D.; Ozin, G. A.; Reber, C.; Pelletier, Y.; Bedard, R. L. *Adv. Mater.* **1997**, *9*, 1133.

(13) Beattie, I. R.; Gilson, T.; Livingstone, K.; Fawcett, V.; Ozin, G. A. *J. Chem. Soc. A* **1967**, 712.

(14) Creighton, J. A.; Green, J. H. S. *J. Chem. Soc. A* **1968**, 808.

(15) Huheey, J. E. *Inorganic Chemistry*, 3rd ed.; Harper & Row: New York, 1983.

(16) Rossi, A. R.; Hoffmann, R. *Inorg. Chem.* **1975**, *14*, 365.

(17) Harrison, P. G. *Chemistry of Tin*; Chapman and Hall: New York, 1989.

(18) Mundus, C.; Taillades, G.; Pradel, A.; Ribes, M. *Solid State Nucl. Magn. Reson.* **1996**, *7*, 141.

(19) Hartree, D. R. *Proc. Cambridge Philos. Soc.* **1928**, *24*, 89.

(20) Fock, V. *Z. Phys.* **1930**, *61*, 126.

(21) Frisch, M. J.; Trucks., G. W.; Head-Gordon, M.; Gill, P. M. W.; Wong, M. W.; Foresman, J. B.; Johnson, B. G.; Schlegel, H. B.; Robb, M. A.; Replogle, E. S.; Gomperts, R.; Andres, J. L.; Raghavachari, K.; Binkley, J. S.; Gonzalez, C.; Martin, R. L.; Fox, D. J.; Defrees, D. J.; Baker, J.; Stewart, J. J. P.; Pople, J. A. *Gaussian92*, Revision C; Gaussian Inc.: Pittsburgh, PA, 1992.

(22) Dag, Ö.; Ahari, H.; Ozin, G. A. Unpublished results.

(23) Jiang, T.; Ozin, G. A.; Bedard, R. L. *Adv. Mater.* **1994**, *6*, 860. Jiang, T.; Lough, A. J.; Bedard, R. L.; Ozin, G. A. *J. Mater. Chem.*, in press.

(24) Thompson, A. H.; Whittingham, M. S. *Mater. Res. Bull.* **1977**, *12*, 741.

(25) Tributsch, H. *Adv. Chem. Phys.* **1982**, *49*, 128.

(26) Kubelka, P.; Munk, F. *Z. Tech. Phys.* **1931**, *12*, 593. Kubelka, P. *J. Opt. Soc. Am.* **1948**, *38*, 448. Frie, R. W.; MacNeil, J. D. *Diffuse Reflectance Spectroscopy in Environment Problem Solving*; CRC Press: Cleveland, 1973.

(27) Domingo, G.; Itoga, R. S.; Kannewurf, C. R. *Phys. Rev.* **1966**, *143*, 536. Lee, P. A.; Said, G.; Davis, R.; Lim, T. H. *J. Phys. Chem. Solids* **1969**, *30*, 2719. Camassel, J.; Schlüter, M.; Kohn, S.; Voitchovsky, J. P.; Shen, Y. R.; Cohen, M. L. *Phys. Status Solidi B* **1976**, *75*, 303. Au-Yang, M. Y.; Cohen, M. L. *Phys. Rev.* **1969**, *178*, 1279.

(28) Shibata, T.; Kambe, N.; Muranushi, Y.; Miura, T.; Kishi, T. *J. Phys. D: Appl. Phys.* **1990**, *23*, 719. Greenway, D. L.; Nitsche, R. *J. Phys. Chem. Solids* **1965**, *26*, 1445. Lee, P. A.; Said, G. *J. Phys. D* **1968**, *1*, 837.

(29) Burns, G. *Solid State Physics*; Academic Press Inc.: Toronto, 1985.

(30) Reed, M. A. *Sci. Am.* **1993**, January, 118.

(31) Ahari, H.; Verma, A.; Ozin, G. A. Unpublished results.

(32) Vegard, L. *Z. Phys.* **1921**, *5*, 17. Lee, S.; Miyazaki, H.; Mahanti, S. D.; Solin, S. A. *Phys. Rev. Lett.* **1989**, *62*, 3066. Kim, D. *J. Am. Ceram. Soc.* **1989**, *72*, 1415.

(33) Hoffmann, R. *Solids and Surfaces, A Chemist's View of Bonding in Extended Structures*; VCH Publishers: New York, 1988.